Draft version February 28, 2019
Preprint typeset using LaTeX style emulateapj v. 08/22/09

SPECTRAL MAGNETIC HELICITY OF SOLAR ACTIVE REGIONS BETWEEN 2006 IN 2017

Sanjay Gosain[1] & Axel Brandenburg[2,3,4,5]
[1]National Solar Observatory, 3665 Discovery Drive, Boulder, CO 80303, USA
[2]Nordita, KTH Royal Institute of Technology and Stockholm University, Roslagstullsbacken 23, SE-10691 Stockholm, Sweden
[3]Department of Astronomy, AlbaNova University Center, Stockholm University, SE-10691 Stockholm, Sweden
[4]JILA and Laboratory for Atmospheric and Space Physics, University of Colorado, Boulder, CO 80303, USA
[5]McWilliams Center for Cosmology & Department of Physics, Carnegie Mellon University, Pittsburgh, PA 15213, USA
(Revision: 1.33)
Draft version February 28, 2019

ABSTRACT

We compute magnetic helicity and energy spectra from about 2500 patches of 100 Mm side length on the solar surface using data from Hinode during 2006–2017. An extensive database is provided where we list magnetic energy and helicity, large- and small-scale magnetic helicity, mean current helicity density, fractional magnetic helicity, and correlation length along with the Hinode MapID, as well as Carrington latitude and longitude of the active region (AR). Significant departures from the hemispheric sign rule are apparent, which is argued to be a physical effect associated with the dominance of individual ARs. In comparison with earlier work, the typical correlation length is found to be between six and eight megameters (Mm), while the length scale relating magnetic and current helicity to each other is found to be around 1.4 Mm.

Subject headings: Sun: magnetic fields — dynamo — magnetohydrodynamics — turbulence

1. INTRODUCTION

The Sun's global magnetic field is produced by a large-scale dynamo where the overall rotation and vertical density stratification are believed to play important roles in driving what Parker (1955) called cyclonic convection. This means that the flow has a swirl, which can be quantified by its kinetic helicity. Although the details of the solar dynamo are still being debated, there is no doubt that also the Sun's magnetic field possesses helicity. This was first found by Seehafer (1990), who determined the swirl of electric current lines, i.e., the current helicity, as the product of the vertical components of magnetic field and current density. Its value was found to be predominantly negative in the northern hemisphere and positive in the southern.

Subsequent work by Pevtsov et al. (1995) confirmed the overall hemispheric dependence, but also showed significant scatter. The work of Bao & Zhang (1998) using the Huairou Solar Observing Station of the Beijing Astronomical Observatory also showed scatter, but it was less than what was found by Pevtsov et al. (1995).

The study of solar magnetic helicity received widespread attention with the Chapman Conference in Boulder/Colorado during July 28–31, 1998 (Brown et al. 1999). Nowadays, the most commonly employed methods include the determination of mean current helicity, the $\alpha_{\rm ff}$ parameter in the force-free field extrapolation, and the gauge-invariant magnetic helicity of the reconstructed force-free magnetic field in the volume above an active region. More recently, there has been growing interest in measuring magnetic helicity *spectra* for selected patches at the solar surface. The integral of these spectra over all wavenumbers gives the mean magnetic helicity density in the Coulomb gauge. Furthermore, the integrated magnetic helicity spectrum weighted with a k^2 factor gives the mean current helicity density based on the vertical components of current density and magnetic field in that patch. Unlike the magnetic helicity, it is gauge-independent, but also expected to be more sensitive to noise resulting from the k^2 factor, which amplifies the contributions from high wavenumbers k, i.e., the small-scale contributions that are often less accurate.

Thus, an important advantage of the spectral approach is that it allows us to filter out certain wavenumber contributions. This is the approach adopted in the present paper. Another advantage of the spectral approach is that it allows us to determine the fractional helicity, which is a non-dimensional measure of the relative amount of magnetic helicity that can give us a sense of the reliability or importance of a particular measurement. For example, one might want to discard all measurements for which the fractional helicity is less than a certain percentage of the maximum possible value.

Finally, we can determine the typical correlation length of the magnetic field, which corresponds to the integral over the spectrum weighted by k^{-1} and normalized by the mean magnetic energy density. Again, it can be used as a threshold if we are only interested in large active regions, for example.

In a few selected cases, the measurement of magnetic helicity spectra has revealed systematic sign changes separately for large and small scales. An example is AR 11515, which emerged in the southern hemisphere, but was found to violate the hemispheric sign rule (Lim et al. 2016). The spectral analysis showed that this sign rule violation occurred at large scales, while the small scale magnetic helicity still obeyed the hemispheric sign rule. This "bihelical" nature of the field was an interesting aspect that is actually expected based on dynamo they (Seehafer 1996; Ji 1999; Blackman & Brandenburg 2003). Scale-dependent sign changes of magnetic helicity have been found also in the solar wind (Brandenburg et al. 2011) and at the solar surface (Singh et al. 2018).

Here we provide an extensive study of many of the publicly available magnetograms of Hinode, which have

a pixel resolution of about 220 km on the Sun. Its resolution is much better than that of the Helioseismic and Magnetic Imager (HMI) on the *Solar Dynamics Observatory*, even though the pixel size in megameters is not so different. One must keep in mind, however, that Hinode is not a survey instrument and that observations exist only for selected patches on the Sun. In an associated online catalogue, we provide for each of the Hinode map identification numbers the mean magnetic energy, mean magnetic helicity, its large- and small-scale contributions, the current helicity, fractional helicity, and the correlation length for about 2500 maps.

2. METHOD

Following the approach of Zhang et al. (2014) and Zhang & Brandenburg (2018), we compute the magnetic helicity spectrum as

$$H_{\rm M}(k) = \tfrac{1}{2} \sum_{k_-<|\boldsymbol{k}|\le k_+} (\tilde{A}_z \tilde{B}_z^* + \tilde{A}_z^* \tilde{B}_z), \quad (1)$$

where $\tilde{B}_i(\boldsymbol{k},t) = \int B_i(\boldsymbol{x},t)\, e^{i\boldsymbol{k}\cdot\boldsymbol{x}} d^2\boldsymbol{x}$ is the Fourier transform of the three magnetic field components $i = x$, y, and z on a two-dimensional Cartesian patch on the Sun with $\boldsymbol{x} = (x, y)$ denoting the position vector, $k_\pm = k \pm \delta k/2$ are the wavenumbers of an interval of width $\delta k = 2\pi/L$ around k in the plane with the area L^2 and L being the size of the magnetograms, and

$$\tilde{A}_z = (-ik_x \tilde{B}_y + ik_y \tilde{B}_x)/k^2 \quad (2)$$

is the vertical component of the Fourier-transformed magnetic vector potential.

We define the total magnetic energy spectrum in the plane as

$$E_{\rm M}(k) = \tfrac{1}{2} \sum_{k_-<|\boldsymbol{k}|\le k_+} |\tilde{B}_x(\boldsymbol{k})|^2 + |\tilde{B}_y(\boldsymbol{k})|^2 + |\tilde{B}_z(\boldsymbol{k})|^2. \quad (3)$$

As in Zhang et al. (2014), it will be interesting to compare with the contributions from the horizontal and vertical fields, $E_{\rm M}^{\rm (h)}$ and $E_{\rm M}^{\rm (v)}$, respectively, which were defined such that, if the two were equal to each other, they would both be an approximation to the total energy, i.e., $E_{\rm M}(k) \approx E_{\rm M}^{\rm (h)} \approx E_{\rm M}^{\rm (v)}$, which requires that we define the individual contributions such that

$$E_{\rm M}^{\rm (h)} + E_{\rm M}^{\rm (v)} = 2E_{\rm M}(k). \quad (4)$$

Specifically, we thus define them as

$$E_{\rm M}^{\rm (h)}(k) = \sum_{k_-<|\boldsymbol{k}|\le k_+} |\tilde{B}_x(\boldsymbol{k})|^2 + |\tilde{B}_y(\boldsymbol{k})|^2, \quad (5)$$

$$E_{\rm M}^{\rm (h)}(k) = \sum_{k_-<|\boldsymbol{k}|\le k_+} |\tilde{B}_z(\boldsymbol{k})|^2, \quad (6)$$

$$(7)$$

i.e., without the 1/2 factor so that Equation (4) is obeyed.

With our approach, we obtain the mean magnetic energy and helicity densities in the plane as

$$\mathcal{E}_{\rm M} = \int_0^\infty E_{\rm M}(k)\, dk, \quad \mathcal{H}_{\rm M} = \int_0^\infty H_{\rm M}(k)\, dk. \quad (8)$$

Since most of the magnetic energy and helicity in the plane comes from the active region and not the space around it, it makes sense to multiply $\mathcal{E}_{\rm M}$ and $\mathcal{H}_{\rm M}$ by the size of the patch, L^2. Furthermore, to facilitate comparison with results in the literature, Zhang et al. (2014) chose to compute energy and helicity over an arbitrarily defined volume of height $L_z = 100\,{\rm Mm}$ above the active region. We adopt here the same approach and thus quote the values of

$$e_{\rm M} = \mathcal{E}_{\rm M} L^2 L_z, \quad h_{\rm M} = \mathcal{H}_{\rm M} L^2 L_z. \quad (9)$$

We also determine the large-scale (LS) and small-scale (SS) contributions to the magnetic helicity by defining

$$\mathcal{H}_{\rm M}^{\rm LS} = \int_0^{k_{\rm LS}} H_{\rm M}(k)\, dk, \quad \mathcal{H}_{\rm M}^{\rm SS} = \int_{k_{\rm SS}}^\infty H_{\rm M}(k)\, dk, \quad (10)$$

where we chose $k_{\rm LS} = 0.4\,{\rm Mm}^{-1}$ and $k_{\rm SS} = 3\,{\rm Mm}^{-1}$ as the limiting wavenumbers marking the end of the LS range and the beginning of the SS range, respectively. This choice can be motivated by inspecting several examples of spectra that show similar signs of spectral magnetic helicity in the ranges $k < k_{\rm LS}$ and $k > k_{\rm SS}$.

As alluded to above, we also compute the correlation length of the magnetic field, which is defined as

$$\ell_{\rm M} = \int_0^\infty k^{-1} E_{\rm M}(k)\, dk \Big/ \int_0^\infty E_{\rm M}(k)\, dk. \quad (11)$$

This allows us to compute the fractional helicity as

$$r_{\rm M} = \mathcal{H}_{\rm M}/2\ell_{\rm M}\mathcal{E}_{\rm M}. \quad (12)$$

The value of $r_{\rm M}$ lies in the range $-1 \le \ell_{\rm M} \le 1$.

3. OBSERVATIONAL DATA

We use high resolution and high-sensitivity vector magnetograms provided as level-2 data products by the Milne-Eddington inversion pipeline MERLIN at HAO/CSAC (DOI:10.5065/D6JH3J8D). These vector magnetograms are deduced from the spectropolarimetric scans of solar magnetic regions by the Hinode SOT/SP instrument that has a diffraction limited field-of-view of up to $328'' \times 164''$ and an angular resolution of 0.3 arcsec. The level-2 data products consist of area scans of a variety of target regions such as active regions, quiet sun, polar regions, and repeated small region scans for time evolution studies. For our study we down-selected these data to include only active regions and pores. The level-2 vector magnetograms were resolved for 180° azimuth ambiguity using the method described in Rudenko & Anfinogentov (2014).

We selected the data based on the following criteria:

- The observed region should be inside the heliocentric angle range of 0 to 30 degrees. This is done to avoid perspective effects and the need to do a heliographic coordinate transformation of the vector magnetograms.
- The field-of-view of the observed region should be at least $96''$ in either direction. This is done to avoid partial/incomplete scans of active regions.
- The total area occupied by dark umbra or pores in the observed region should be greater than $(10'')^2$, or 900 pixels. This is done to avoid selecting very

small-sized pores. The umbral area is computed from the continuum intensity map by first removing the limb darkening function and then normalizing the intensity to median value in non-magnetic pixels. Pixels with normalized intensity less than or equal to 0.55 are treated as umbra or pore.

- The data that satisfies the above criteria sometimes include undesired characteristics such as repeated small area scans for time evolution studies of sunspots or active region scans with missing scan lines, bad columns, or partial scans. Thus, as a final criterion, the data is displayed and manually rejected if these undesired characteristics are present.

The distribution of latitude, longitude and year of the selected observations is shown in Figure 1. It is found to be relatively uniform, except for the time of solar minimum during 2008 and 2009.

Hinode observes the target regions with either normal mode (0.16″/pixel sampling) or fast mode (0.32″/pixel sampling). In our selected dataset, both modes exist. We convert normal mode scans in our dataset to 0.32″/pixel, so that all maps have the same spatial sampling. Further, in our calculations we always use 512×512 pixels in the region-of-interest (ROI). If the original data is larger, we extract 512×512 ROI centered pixels around the active region or pore. On the other hand, if the original data is smaller, we embed the observed region in the center of a 512×512 array with zero padding in adjacent missing pixels.

Finally, we create a database[1] of helicity parameters for each scan, which is uniquely identified by the Hinode MapID.

4. RESULTS

We have processed 2499 vector-magnetograms over the solar disc. We have produced a database for 1000 active regions during the years 2006 to 2017, covering in some cases the entire evolution of an active region as it passes the solar disc. There can be significant temporal variations of helicity, which are sometimes associated with the development of flares and coronal mass ejections.

4.1. *Time-Latitude Distribution of Helicity*

Hinode data selected here span almost a solar cycle so we first look at the distribution of helicity sign and magnitude with time and latitude during end of cycle 23 and most of the cycle 24. In Figure 2, the distribution of $H_{\rm M}$, $H_{\rm C}$ and $r_{\rm M}$ are given. The negative (positive) sign of these parameters are represented by blue (red) color. As is found in many previous studies the statistical trend of negative (positive) sign in the northern (southern) hemisphere is present. The relative amplitude of these parameters is represented by radius of the circle symbol in Figure 2. We summarize the hemispheric statistics of these parameters in Table 1 with 95% confidence intervals. It is seen that hemispheric bias is present and is significant in $h_{\rm M}$, $h_{\rm M}^{\rm LS}$, and $r_{\rm M}$ in both hemispheres. While for current helicity ($\mathcal{H}_{\rm C}$) the bias is weak in the north but strong in the south. For small scales, $h_{\rm M}^{\rm SS}$ shows a peculiar result in that the sign is predominantly positive in both north (75%) and south (83%). This is perhaps because (as seen in Table 2) most of the helicity is accounted for by the large-scale component. Typically, for all of the data the amplitude of small-scale helicity is about 10^4 times smaller than large scale helicity. Thus, most of the contribution might be coming from noise in the data. There is good agreement between $h_{\rm M}$, $h_{\rm M}^{\rm LS}$ and $r_{\rm M}$ statistics.

[1] http://www.nordita.org/ brandenb/projects/Hinode

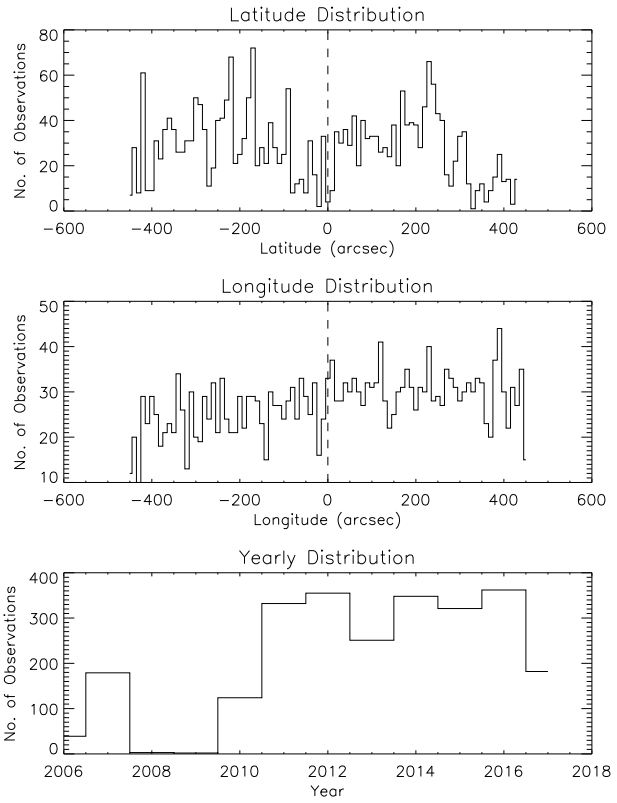

FIG. 1.— Distribution of Hinode observations selected for this study in latitude, longitude and year-wise shown in top, middle and bottom panel, respectively.

TABLE 1
PERCENT OF ACTIVE REGIONS FOLLOWING HEMISPHERIC RULE

Hemisph.	$h_{\rm M}$[%]	$h_{\rm M}^{\rm LS}$[%]	$h_{\rm M}^{\rm SS}$[%]	$\mathcal{H}_{\rm C}$[%]	$r_{\rm M}$[%]
North	63±3	63±3	25±2	49±3	63±3
South	59±3	58±3	83±2	73±2	59±3

4.2. *Latitudinal dependence*

The dependence of the fractional magnetic helicity on latitude is shown in Figure 3. This relation is extremely noisy, although there is still a clear negative correlation with latitude. Specifically, we find

$$r_{\rm M}(\lambda) = -0.002 - 0.055 \sin\lambda. \qquad (13)$$

The dependences of $\mathcal{H}_{\rm M}(t)$ and $\mathcal{H}_{\rm C}(t)$ on latitude (not shown) are even more noisy, but they also show negative

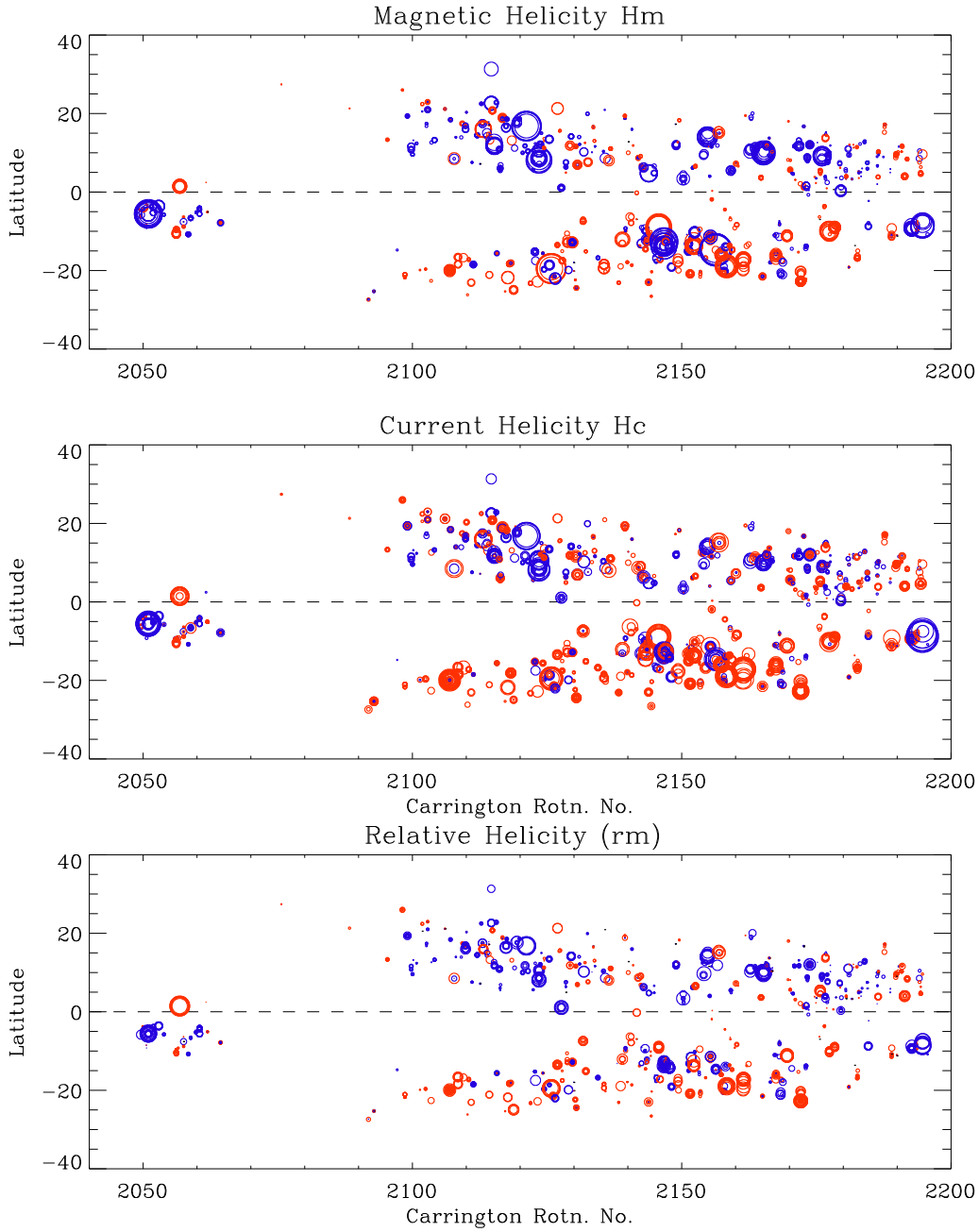

FIG. 2.— Time-latitude distribution of helicity parameters. Top panel shows the distribution of magnetic helicity density (H_m), middle panel the current helicity density (H_c), and the bottom panel shows the relative helicity (r_m). The blue (red) circles represents negative (positive) sign of these parameters while the diameter of circles represents relative amplitude (scaled between ± 1).

correlations:

$$h_{\rm M}(\lambda) = -0.45 - 0.93 \sin\lambda \quad [{\rm G}^2\,{\rm Mm}^4], \qquad (14)$$

$$\mathcal{H}_{\rm C}(\lambda) = 24 - 41 \sin\lambda \quad [{\rm G}^2\,{\rm km}^{-1}]. \qquad (15)$$

This is rather surprising and seems to support a similar trend from earlier findings that at higher resolution, the general hemispheric sign rule deteriorates; cf. the earlier findings by Bao & Zhang (1998) and Pevtsov et al. (1995), where the latter showed much stronger scatter than the former.

4.3. *Time dependence*

There is a general hemispheric preference with most of the active regions having negative magnetic helicity in the north and positive in the south. However, there can also be significant departures from this hemispheric preference. Figure 4 shows the evolution of $\mathcal{E}_{\rm M}(t)$, $\mathcal{H}_{\rm M}(t)$, $\ell_{\rm M}(t)$, and $r_{\rm M}(t)$ for all 2499 maps, regardless of position or selection effects arising from the fact that particularly interesting active regions have been observed

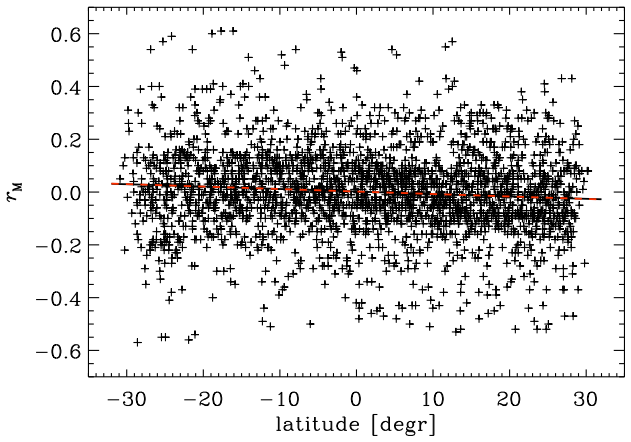

FIG. 3.— Dependence of fractional magnetic helicity on latitude.

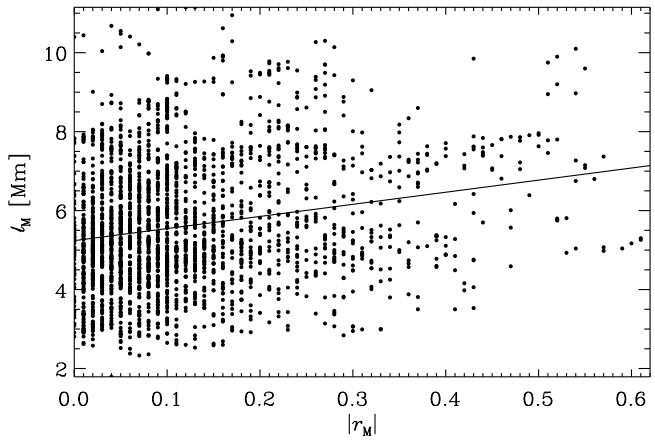

FIG. 5.— Scatter plot between $r_M(t)$ and $\ell_M(t)$.

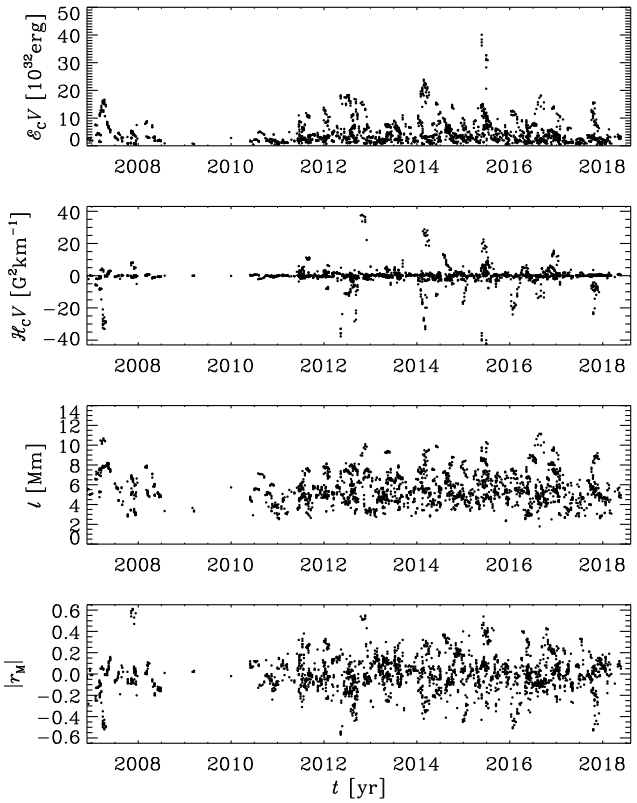

FIG. 4.— Temporal variation of $\mathcal{E}_M(t)$, $\mathcal{H}_M(t)$, $\ell_M(t)$, and $r_M(t)$ for all 2499 maps.

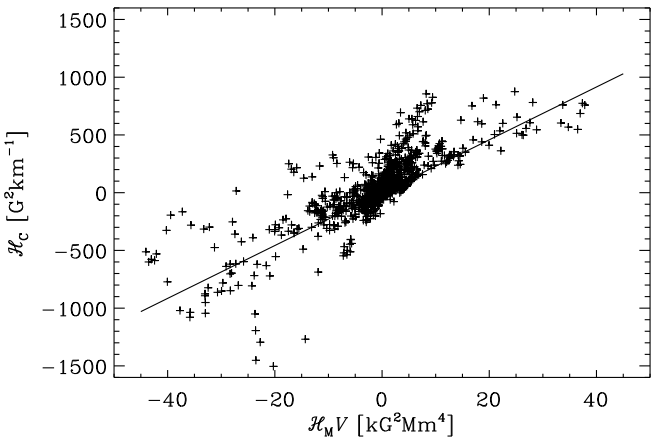

FIG. 6.— Scatter plot showing the dependence of small-scale magnetic helicity on magnetic helicity.

repeatedly. One clearly sees overall enhanced activity during solar maximum around 2014 and only very few measurements during solar minimum around 2008 and 2009. While $\mathcal{E}_M(t)$ shows some intense spikes of activity on the timescale of 1–2 years, the spikes in $|\mathcal{H}_M(t)|$ are even more extreme. This is reminiscent of earlier findings using a related method applied to synoptic vectormagnetograms (Brandenburg et al. 2017). On the other hand, $r_M(t)$ seems to be now less spiky than what has been found from the synoptic vectormagnetograms. This difference can well be caused by the aforementioned selection effects resulting from the fact that particularly interesting regions have been observed more frequently.

The overall variation of $\ell_M(t)$ is rather small and the values are around 6 Mm both during minimum and maximum. Similar values have also been found with both HMI and the Huairou Solar Observing Station (Zhang et al. 2016). This value of ℓ_M is significantly smaller than what has been found using the synoptic vectormagnetograms from HMI, where ℓ_M was found to fluctuate around 20 Mm, or from the synoptic vectormagnetograms from SOLIS, where ℓ_M was found to fluctuate around 15 Mm (Singh et al. 2018).

As already noticed by Singh et al. (2018), the numerical value of ℓ_M must not be interpreted as a physically identifiable length scale. In fact, since it is defined as a weighted inverse wavenumber, it makes sense to identify $2\pi\ell_M$ with a physically relevant length scale.

The fact that ℓ_M is about three times larger when it is determined from the synoptic maps is interesting and has not previously been noticed. This may indicate that a synoptic magnetogram is different from an actual magnetogram. It could be caused by an anisotropy resulting from the assembly of different magnetograms in the longitudinal direction that has not previously been appreciated.

Earlier work by Zhang et al. (2016) showed that $\ell_M(t)$

displays a clear modulation with the solar cycle, where $\ell_{\rm M}(t)$ varied between 6 Mm during solar minimum and 8 Mm during solar maximum. No such clear variation can be seen from our current data. Nevertheless, looking at a scatter plot between $r_{\rm M}(t)$ and $\ell_{\rm M}(t)$ does suggest a positive, albeit very noisy correlation between the two; see Figure 5.

4.4. *Relation with current helicity*

In homogeneous turbulence, there is a relation between the magnetic helicity spectrum and the current helicity spectrum such that $H_{\rm C}(k) = k^2 H_{\rm M}(k)$. There is no such clear relationship between magnetic and current helicity in physical space, although the two could still related to each other by the square of a length scale.

In Figure 6 we show the dependence of small-scale magnetic helicity on current helicity as a scatter plot. We see a positive dependence with a slope $23 \times 10^{-6}\,{\rm Mm}^{-5}$. Adopting again our reference volume of $V = (100\,{\rm Mm})^3$ used in our calculations of $H_{\rm M}(k)$, we find $k^2 = 23\,{\rm Mm}^{-2}$, i.e., $k = 4.8\,{\rm Mm}^{-1}$ or $2\pi/k = 1.3\,{\rm Mm}$. This corresponds to the scale of granulation. Such an association between the typical scale of current helicity patterns and granulation has not previously been possible to make.

4.5. *Case Study: NOAA 10930*

We show in Table 2 the tabulated value of various parameters for the well studied active region NOAA 10930 during December 2006. An example of helicity and energy spectra for this active region during 12 December 2006 at 20:30 UT is shown in Figure 7. We find that the magnetic helicity for this active region is negative during 9 through 13 December 2006. This sign is opposite to the expectation from the hemispheric helicity rule. Negative sign is shown by all helicity indicators in Table 2 except small scale magnetic helicity, $h_{\rm M}^{\rm SS}$, during 9 December 12:40 UT to 10 December 10:55 UT.

The AR was flare productive and led to 3 M-class, 3 X-class, and several C-class flares. Many authors have reported strong rotating motion in one of the spots in this group (Yan et al. 2009). Using the three dimensional (3D) nonlinear force-free field (NLFFF) extrapolation method, Park et al. (2010) computed the relative coronal magnetic helicity for this active region to be about -4.3×10^{43} Mx^2 just before X3.4 flare on 13 December 2006. In comparison, our magnetic helicity estimate, $h_{\rm M}$, for this time is about -2.6×10^{43} Mx^2. We notice that the time of peak helicity in this active region from Park et al. (2010) and our estimates is the same, i.e., around 3:50 to 10:10 UT on 12 December 2006. Park et al. (2010) suggest that the evolution of helical structures of opposite sign to the AR dominant helicity sign led to flaring activity in this active region.

Ravindra et al. (2011) studied the evolution of net electric currents in this active region and found that dominant current in the two opposite magnetic polarities is of opposite sign, i.e., upward electric current in one polarity and downward in another. Further, they found that the net current in both polarities decreases before the flares and attributed this decrease to an increase in the non-dominant opposite signed current in each polarity.

The helicity spectra in the top panel of Figure 7 do show helicity of both signs in general, but the dominant sign is negative when averaged over logarithmically spaced wavenumber bins. The evolution of the such helicity spectra at different scales and their relationship with flaring and/or eruptive activity could be insightful. We defer such study in flaring regions for a future work.

4.6. *Spectral energy for vertical and horizontal fields*

It is instructive to look at magnetic energy spectra separately for horizontal and vertical (or radial) magnetic fields. The two are remarkably similar at all wavenumbers; see Figure 7. This is rather different from the earlier results by Zhang et al. (2014)[2], who found significant departures at small scales where the horizontal contribution was found to exceed the vertical one by a factor of about three.

The reason for the small-scale excess of horizontal over vertical field strengths may well be physical, but it is striking that with the higher resolution of Hinode, the two spectra track each other much better than with Hinode. Looking at Figure 7, the two spectra agree nearly perfectly up to $k = 10\,{\rm Mm}^{-1}$, which corresponds to a scale of $(2\pi/10)\,{\rm Mm} \approx 600\,{\rm km}$. This leads us to expect that with even higher resolution such as that of Daniel K. Inouye Solar Telescope, we may continue to see the two spectra tracking each other up to larger wavenumbers at higher resolution. It also suggests that, if we regard the wavenumber where the spectra depart from each other as the resolution limit, this limit is poorer than previously anticipated. Indeed, with HMI, we see departures already at scales of around 2 Mm. Much of this departure is actually caused by intrinsic artifacts that could be accounted for in subsequent analyzes.

5. CONCLUSIONS

The purpose of the present work was to use Hinode data to provide a comprehensive survey of spectral magnetic helicity. The data turn out to be of considerably higher quality than those used in earlier analyzes using HMI and SOLIS data. This became evident when comparing the magnetic energy spectra separately for vertical and horizontal magnetic field components. Unlike earlier work using HMI, which showed significant departure between the two, the present analysis results in a rather different characteristics, with the two spectra tracking each other up $k = 10\,{\rm Mm}^{-1}$, while earlier work of Zhang et al. (2014) showed departures between the two already at $k = 3\,{\rm Mm}^{-1}$.

The correlation length $\ell_{\rm M}$, on the other hand, appears to be rather similar between current and earlier analyzes, although there are differences in comparison with similar results using synoptic magnetograms. Those differences are tentatively associated with the anisotropy resulting from combining magnetograms of different times into a new map.

A major surprise arising from our work is the poor obedience of the hemispheric sign rule of both magnetic and current helicity. We argued before that magnetic helicity should be much less affected by noise than the current helicity, but this is not really supported by the current data.

[2] We use here the opportunity to correct a labeling error in their Figure 2 where the energies of vertical and horizontal fields should have been swapped.

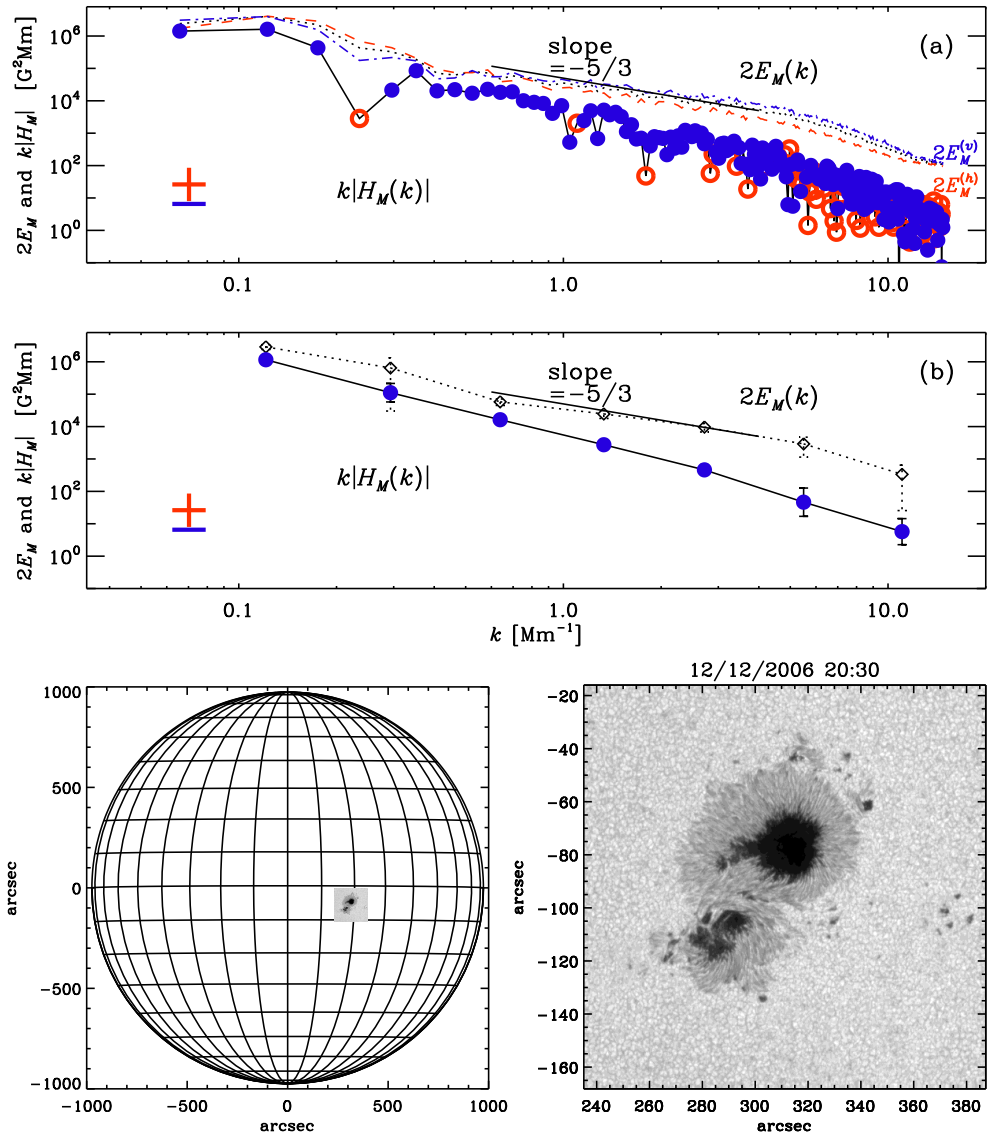

FIG. 7.— (a) $2E_{\rm M}(k)$ (dotted line) and $k|H_{\rm M}(k)|$ (solid line) for NOAA 10930 at 20:30 UT on 2006 December 12. Positive (negative) values for $H_{\rm M}(k)$ are indicated by open (closed) symbols, respectively. $2E_{\rm M}^{(h)}(k)$ (red, dashed) and $2E^{(v)}{}_{\rm M}(k)$ (blue, dash-dotted) are shown for comparison. (b) Same as (a), but the magnetic helicity is averaged over broad logarithmically spaced wavenumber bins.

The reason for this is not at all obvious. Looking for example at the case of AR 10900, we see that the spectrum is not actually very noisy, but that it has the same sign at almost all wavenumbers. Moreover, AR 10900 was located in the southern hemisphere, but had the same sign as that expected normally in the northern hemisphere. This may then suggest that the hemispheric sign rule violations are not connected with measurement uncertainties, but they may instead be physical. While this is a plausible proposal, it remains curious as to why much weaker fluctuations are generally seen at poorer resolution. One possibility is that there could be significant systematic errors that tend to produce magnetic helicity in agreement with the hemispheric sign role. The most extreme evidence of this comes from the results of the analysis of synoptic magnetograms (Brandenburg et al. 2017; Singh et al. 2018), where very little departure from is the hemispheric sign rule has been found. In some cases, there are even wavenumber-dependent sign reversals of magnetic helicity that agreed with theoretical expectations. Such an interpretation would not only be disappointing, but it will also raise the question of what is the nature of such systematic errors that produce, or reproduce, the expected sign role.

REFERENCES

Bao, S.. & Zhang, H. 1998, ApJ, 496, L43
Brown, M. R., Canfield, R. C., & Pevtsov, A. A. 1999, Magnetic Helicity in Space and Laboratory Plasmas (Geophys. Monograph **111**, American Geophysical Union, Florida)
Blackman, E. G., & Brandenburg, A. 2003, ApJL, 584, L99
Brandenburg, A., Petrie, G. J. D., & Singh, N. K. 2017, ApJ, 836, 21

TABLE 2
Summary of data for AR 10930.

y	m	d	h:m	$e_{\rm M}$	$h_{\rm M}$	$h_{\rm M}^{\rm LS}$	$h_{\rm M}^{\rm SS}$	$\mathcal{H}_{\rm C}$	$r_{\rm M}$	$\ell_{\rm M}$	λ	$\mathcal{L}$	MapID
2006	12	9	10:00	10.8	−8.8	−8.8	−2.3	−202	−0.22	7.56	−5.7	−26.9	30107
2006	12	9	11:20	11.0	−8.7	−8.7	−5.5	−179	−0.21	7.57	−5.7	−26.3	30108
2006	12	9	12:40	11.1	−8.6	−8.5	2.7	−157	−0.20	7.64	−5.7	−25.5	30109
2006	12	9	14:00	11.2	−8.0	−8.0	4.8	−140	−0.19	7.60	−5.7	−24.8	30110
2006	12	9	17:10	11.3	−8.1	−8.1	10.7	−117	−0.19	7.61	−5.7	−23.0	30111
2006	12	9	22:00	11.8	−8.1	−8.0	11.9	−128	−0.18	7.61	−5.7	−20.4	30112
2006	12	10	1:00	12.1	−8.1	−8.0	4.9	−144	−0.17	7.62	−5.7	−18.7	30113
2006	12	10	10:55	13.7	−8.2	−8.2	6.4	−197	−0.16	7.44	−5.7	−12.6	30114
2006	12	10	21:00	14.4	−14.7	−14.5	−4.4	−489	−0.27	7.66	−5.7	−7.6	30115
2006	12	11	3:10	15.2	−20.9	−20.7	−14.7	−720	−0.35	7.73	−5.7	−4.1	30116
2006	12	11	8:00	15.5	−24.3	−24.0	−11.6	−806	−0.40	7.71	−5.7	−1.5	30117
2006	12	11	11:10	15.6	−26.8	−26.6	−12.1	−802	−0.44	7.84	−5.7	0.4	30118
2006	12	11	13:10	15.7	−28.3	−28.0	−10.6	−848	−0.46	7.81	−5.7	1.9	30119
2006	12	11	17:00	16.2	−29.9	−29.7	−6.4	−850	−0.47	7.87	−5.7	3.5	30120
2006	12	11	20:00	16.2	−30.7	−30.4	−10.8	−862	−0.48	7.86	−5.7	5.2	30121
2006	12	11	23:10	16.2	−32.4	−32.2	−12.7	−822	−0.50	7.92	−5.7	7.0	30122
2006	12	12	3:50	16.7	−33.0	−32.8	−16.7	−892	−0.51	7.78	−5.7	9.6	30123
2006	12	12	10:10	16.3	−33.0	−32.8	−19.2	−875	−0.52	7.80	−5.5	13.6	30124
2006	12	12	15:30	15.8	−29.7	−29.5	−17.1	−781	−0.48	7.77	−5.7	16.0	30125
2006	12	12	17:40	15.6	−28.1	−27.9	−17.5	−696	−0.46	7.81	−5.7	17.2	30126
2006	12	12	20:30	15.0	−25.8	−25.7	−11.2	−596	−0.43	7.88	−5.7	18.8	30127
2006	12	13	4:30	14.8	−29.1	−29.0	−14.1	−638	−0.49	7.91	−5.7	23.2	30128
2006	12	13	7:50	14.2	−28.3	−28.2	−8.7	−618	−0.50	7.96	−5.7	25.1	30129

$h_{\rm M}$ is in 10^{38} Mx^2, while $\mathcal{H}_{\rm C}$ is in ...

Brandenburg, A., Subramanian, K., Balogh, A., & Goldstein, M. L. 2011, ApJ, 734, 9
Ji, H. 1999, Phys. Rev. Lett., 83, 3198
Lim, E.-K., Yurchyshyn, V., Park, S.-H., Kim, S., Cho, K.-S., Kumar, P., Chae, J., Yang, H., Cho, K., Song, D., & Kim, Y.-H. 2016, ApJ, 817, 39
Parker, E. N. 1955, ApJ, 122, 293
Park, S-H., Chae, J., Jing, J., Tan, C. & Wang, H. 2010, 2010, ApJ, 720, 1102
Pevtsov, A. A., Canfield, R. C., & Metcalf, T. R. 1995, ApJ, 440, L109
Ravindra, B., Venkatakrishnan, P., Tiwari, S. K., & Bhattacharyya, R. 2011, ApJ, 740, 19
Rudenko, G. V., & Anfinogentov, S. A. 2014, Sol. Phys., 289, 1499
Seehafer, N. 1990, Solar Phys., 125, 219
Seehafer, N. 1996, Phys. Rev. E, 53, 1283
Singh, N. K., Käpylä, M. J., Brandenburg, A., Käpylä, P. J., Lagg, A., & Virtanen, I. 2018, ApJ, 863, 182
Yan, X.-L., Qu, Z.-Q., Xu, C.-L., Xue, Z.-K., & Kong, D.-F. 2009, Res. Astron. Astrophys., 9, 596
Zhang, H., & Brandenburg, A. 2018, ApJL, 862, L17
Zhang, H., Brandenburg, A., & Sokoloff, D. D. 2014, ApJL, 784, L45
Zhang, H., Brandenburg, A., & Sokoloff, D. D. 2016, ApJ, 819, 146